

IGR J16393–4643: a new heavily-obscured X-ray pulsar

A. Bodaghee^{1,2}, R. Walter^{1,2}, J.A. Zurita Heras^{1,2}, A.J. Bird³, T.J.-L. Courvoisier^{1,2}, A. Malizia⁴, R. Terrier^{5,6}, P. Ubertini⁷

¹ *INTEGRAL* Science Data Centre, Chemin d’Ecogia 16, CH–1290 Versoix, Switzerland

² Observatoire de Genève, Chemin des Maillettes 51, CH–1290 Sauverny, Switzerland

³ School of Physics and Astronomy, University of Southampton, Highfield, Southampton, SO17 1BJ, UK

⁴ IASF/CNR, Via Gobetti 101, I–40129 Bologna, Italy

⁵ CEA-Saclay, DAPNIA/Service d’Astrophysique, F–91191 Gif sur Yvette Cedex, France

⁶ Fédération de recherche APC, Collège de France 11, place Marcelin Berthelot, F–75231 Paris, France

⁷ IASF/CNR, Via Fosso del Cavaliere 100, I–00133 Rome, Italy

Received / Accepted

Abstract. An analysis of the high-energy emission from IGR J16393–4643 (=AX J1639.0–4642) is presented using data from *INTEGRAL* and *XMM-Newton*. The source is persistent in the 20–40 keV band at an average flux of 5.1×10^{-11} ergs cm⁻² s⁻¹, with variations in intensity by at least an order of magnitude. A pulse period of 912.0 ± 0.1 s was discovered in the *ISGRI* and *EPIC* light curves. The source spectrum is a strongly-absorbed ($N_{\text{H}} = (2.5 \pm 0.2) \times 10^{23}$ cm⁻²) power law that features a high-energy cutoff above 10 keV. Two iron emission lines at 6.4 and 7.1 keV, an iron absorption edge ≥ 7.1 keV, and a soft excess emission of 7×10^{-15} ergs cm⁻² s⁻¹ between 0.5–2 keV, are detected in the *EPIC* spectrum. The shape of the spectrum does not change with the pulse. Its persistence, pulsation, and spectrum place IGR J16393–4643 among the class of heavily-absorbed HMXBs. The improved position from *EPIC* is R.A. (J2000)= $16^{\text{h}}39^{\text{m}}05.4^{\text{s}}$ and Dec.= $-46^{\circ}42'12''$ ($4''$ uncertainty) which is compatible with that of 2MASS J16390535–4642137.

Key words. Gamma-rays: observations – X-rays: binaries – pulsars: individuals: IGR J16393–4643, AX J1639.0–4642

1. Introduction

The *INTEGRAL* core program (CP: Winkler et al. 2003) routinely devotes observation time to Galactic Plane Scans (GPS) and Galactic Centre Deep Exposures (GCDE). These numerous snapshots of the Milky Way can be assembled into mosaic images of long exposure time (~ 1 Ms). This gamma-ray view of the galaxy, as collected by *ISGRI* (Ubertini et al. 2003; Lebrun et al. 2003), enabled Bird et al. (2004) to detect 123 sources at a significance above 6σ . Around 20 of these sources are of unknown origin. A good portion of these new sources probably belong to the class of heavily-absorbed High Mass X-ray Binaries (HMXBs) that are concentrated along the galactic plane and in the spiral arms.

High-Mass X-ray Binaries are composed of a compact object such as a neutron star or a black hole that orbits a massive stellar companion. Depending on the type of companion, known HMXBs can be divided into two groups (van Paradijs 1983). Most HMXBs classified by Liu et al. (2000) contain a Be star. These systems are usually transient sources with hard spectra. The compact object has a wide orbit which mostly keeps it away from the Be star and its disk. Outbursts in these systems are due primarily to the compact object approaching

the star and accreting matter from the slow, dense stellar wind. The second group of HMXBs features an O or B supergiant star. The orbit of the compact object places it well within the stellar wind, so material from the supergiant can be fed directly to the compact object through Bondi accretion, or it can pass to the compact object via an accretion disk. The latter mechanism is typically found in bright X-ray binaries in which the Roche lobe overflow of gas from the OB star supercedes the flow of accreting matter. For less luminous binaries, the OB star does not fill its Roche lobe and the behaviour of the X-ray source is determined predominantly by the stellar wind. X-ray emission in supergiant HMXB systems is usually persistent, with flares stemming from inhomogeneities in the wind. Neutron stars with strong magnetic fields develop a hot spot for accretion which can result in a pulsation.

The number of persistent and heavily-absorbed HMXBs associated with supergiant companions has increased thanks to deep, wide-field observations by *INTEGRAL* combined with follow-up X-ray monitoring by *XMM-Newton* (Walter et al. 2003; Rodriguez et al. 2003; Hill et al. 2005; Lutovinov et al. 2005b). So far, these sources have been detected preferentially in the Norma Arm region (Walter et al. 2004) which features high formation rates of OB supergiant stars. It is there that *INTEGRAL* uncovered its first new source,

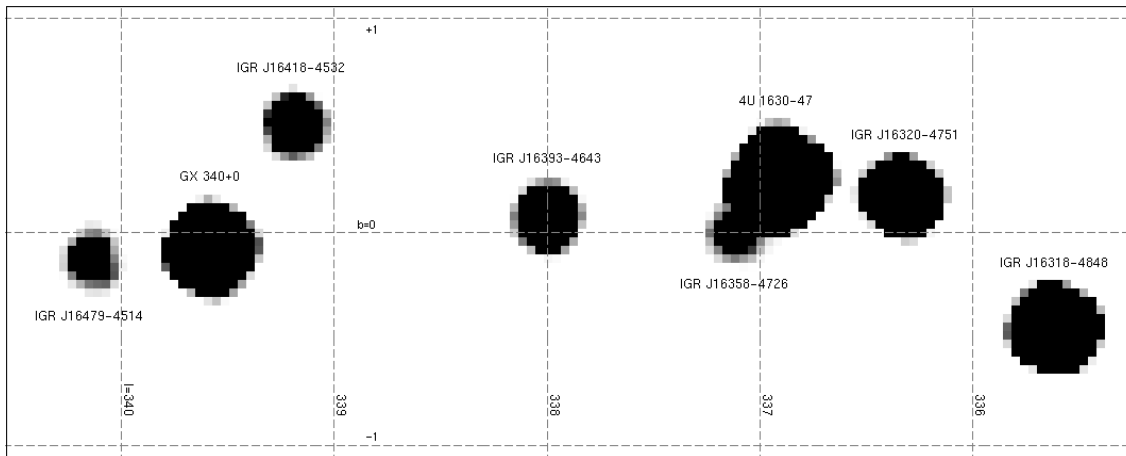


Fig. 1. Intensity map of the Norma Arm in the 20–40 keV band accumulating data from revolutions 30–185 for an effective exposure time of 670 ks. The image is in galactic coordinates and represents an area 2° tall by 5° wide. The galactic equator ($b = 0$) bisects the image horizontally. Neighboring sources from the catalog of Bird et al. (2004) are also shown.

IGR J16318–4848 (Walter et al. 2003). The Norma Arm also harbors IGR J16393–4643. This object was initially discovered in the X-ray band and listed as AX J163904–4642 in the ASCA Faint Source Catalog (Sugizaki et al. 2001). Its flat power-law slope, its absorption ($N_{\text{H}} = 13^{+9}_{-7} \times 10^{22} \text{ cm}^{-2}$), its lack of radio emission, and its position in the galactic plane compelled the authors to classify it as a HMXB. A non-thermal radio counterpart was recently detected in the ASCA error box which suggests a dust-enshrouded microquasar interpretation for the HMXB (Combi et al. 2004), and would help explain the possible association with the unidentified *EGRET* source 3EG J1639–4702 (Hartman et al. 1999) noted by Malizia et al. (2004).

We detected IGR J16393–4643 in the *ISGRI* GPS data of the Norma Arm’s first visibility period, and we obtained a follow-up observation with *XMM-Newton*. The set of *INTEGRAL* and *XMM-Newton* data are introduced in Section 2. In Section 3, the refined X-ray position is used to locate the most likely counterpart at other wavelengths. Timing and spectral analyses are presented in Sections 4 and 5, respectively. Finally, we discuss the nature of the source and we offer our conclusions in Section 6.

2. Observations and Data Sets

2.1. *INTEGRAL* Data and Imaging

The *INTEGRAL* data consist of all CP pointings during revolutions 30–260, as well as pointings that were public by January 3, 2005, which had the source within the *ISGRI* field of view (FOV). To improve the quality of the output mosaic, pointings with exposure times below 1 ks were ignored. The resulting data set groups roughly 1500 pointings with an average exposure time of 2 ks each.

Version 4.2 of the *INTEGRAL* Offline Scientific Analysis (OSA) software was used to reduce raw data into images. Source extraction employed version 18 of the *INTEGRAL* General Reference Catalog (Ebisawa et al. 2003) selected for objects detected by *ISGRI*. These tools are available to the

public through the *INTEGRAL* Science Data Centre (ISDC: Courvoisier et al. 2003).

Intensity, significance, variance, and exposure mosaic images were constructed from background-subtracted images of individual pointings. Figure 1 provides an example of an intensity map of IGR J16393–4643 and its vicinity in the 20–40 keV band from the pointings of revolutions 30 to 185. The effective exposure time is 670 ks after correcting for vignetting. Using this image, we extracted a source location of R.A. (J2000)= $16^{\text{h}}39^{\text{m}}05^{\text{s}}$ and Dec.= $-46^\circ42.3'$ ($26''$ uncertainty) which agrees with and improves the *ISGRI* position of Bird et al. (2004). The mean flux (20–60 keV) of the source is 0.73 ± 0.02 counts per second (cps), or 4.9 mCrab, at a significance of 36σ .

2.2. *XMM-Newton* Data and Imaging

XMM-Newton (Jansen et al. 2001; Strüder et al. 2001; Turner et al. 2001) observed IGR J16393–4643 on March 21, 2004, from 08:21:15 to 11:41:15 (UT). We used the Science Analysis System (SAS) v. 6.1.0 software to analyse the data and to extract the *EPIC* spectrum. The data were screened for background variability by excluding time intervals in which the count rate above 10 keV was greater than a selected threshold (0.33 cps for *EPIC/MOS1*, 0.25 cps for *EPIC/MOS2*, and 2.4 cps for *EPIC/PN*). After screening, the effective exposure times were around 8.4, 8, and 7 ks for *EPIC/MOS1*, *EPIC/MOS2*, and *EPIC/PN*, respectively.

IGR J16393–4643 is clearly detected in images taken by *EPIC*. Figure 2 presents an image of IGR J16393–4643 from the *EPIC/MOS1* camera. Furthermore, the source coincides with the updated *ISGRI* position and error circle from this paper. The refined X-ray position averaged from *EPIC/MOS* and *EPIC/PN* is R.A. (J2000)= $16^{\text{h}}39^{\text{m}}05.4^{\text{s}}$ and Dec.= $-46^\circ42'12''$ ($4''$ uncertainty).

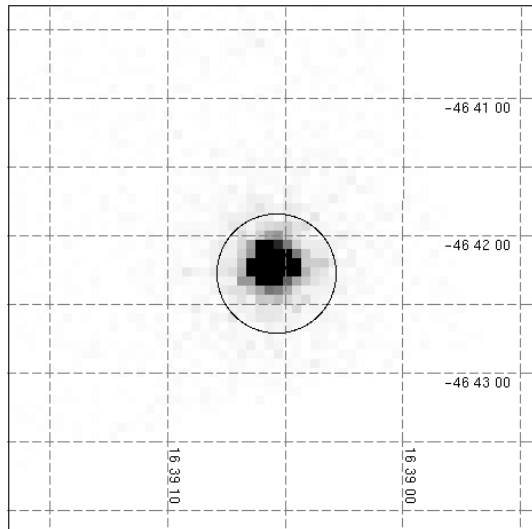


Fig. 2. *EPIC/MOS1* image of IGR J16393–4643 in the 0.15–12 keV energy range with an effective exposure time of 8.4 ks. The refined *ISGRI* error circle from this paper is superimposed.

3. Counterparts

We searched for counterparts at other wavelengths and found a single infrared source belonging to the Two Microns All-Sky Survey (2MASS: Cutri et al. 2003) in the *XMM-Newton* error box. This potential counterpart, 2MASS J16390535–4642137, is located about $2''$ away from the *XMM-Newton* position at R.A. (J2000) = $16^{\text{h}}39^{\text{m}}05.36^{\text{s}}$ and Dec. = $-46^{\circ}42'13.7''$ ($0.06''$ uncertainty). It appears in the *J*, *H*, and *K_s* bands with magnitudes of 14.63 ± 0.06 , 13.32 ± 0.04 , and 12.78 ± 0.04 , respectively (95% confidence).

Figure 3 shows that the *XMM-Newton* position and error radius for IGR J16393–4643 do not intersect the error boxes of the radio source MOST J1639.0–4642 and the far infrared source IRAS 16353–4636, which are the possible counterparts proposed by Combi et al. (2004). The tight *XMM-Newton* error circle excludes optical counterparts from the USNO-B1 catalog (Monet et al. 2003), radio sources from the Vizier database (Ochsenbein et al. 2000), and *ROSAT* sources (Voges et al. 1999).

A possible association of IGR J16393–4643 with the *EGRET* source 3EG J1639–4702 (Hartman et al. 1999) has been proposed by Malizia et al. (2004). Another *ISGRI* source, IGR J16358–4726, and 4U 1630–47 are just outside the *EGRET* 95% error contour. In the $2^{\circ} \times 5^{\circ}$ degree section of the Norma Arm presented in Fig. 1, the probability to observe a counterpart in the 0.56° error radius of the *EGRET* source is close to 1, so the coincidence with IGR J16393–4643 is probably a chance one.

4. Timing Analysis

4.1. Long-term Variability

Most *ISGRI* pointings have exposure times that are too brief for a significant detection. Therefore, a mosaic was prepared for each 3-day spacecraft revolution (from 30–244) in the 20–

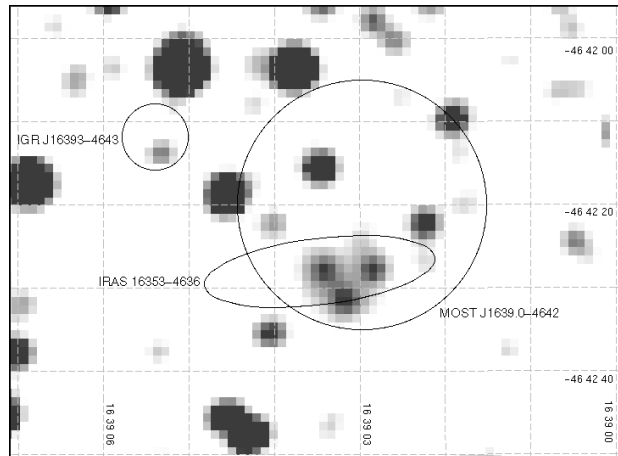


Fig. 3. Image from the 2MASS survey of the region around IGR J16393–4643 in the K_s band. The *XMM-Newton* error circle from this paper does not intersect the error boxes of the radio source MOST J1639.0–4642 and the far infrared source IRAS 16353–4636. The only infrared object inside the *XMM-Newton* error circle is 2MASS J16390535–4642137.

60 and 60–150 keV bands. We extracted the source flux, error, and significance by fitting a Gaussian with a fixed point spread function to the mosaic images. Upper limits (3σ), calculated from the variance maps, are provided when the source is not detected at the 4σ level in a mosaic image with an effective exposure time above 7 ks. There were no detections in mosaic images of the 60–150 keV band so its light curve is omitted.

Figure 4 illustrates the persistence of IGR J16393–4643 in the 20–60 keV energy range. Table 1 collects the 15 revolutions in which the source is detected in the mosaic image with a significance above 4σ . The average flux in these mosaics is 0.86 cps (5.6 mCrab) with a cumulative exposure time of 1.5 Ms. The mean flux per revolution varies by a factor of at least 6 from 0.21 ± 0.05 counts per second (cps) or 1.4 mCrab in revolution 100 (205 ks), to 1.39 ± 0.14 cps (9.3 mCrab) in revolution 55 (96 ks). When the flux value during revolution 100 is compared to the highest flux registered in a single 2-ks pointing of the 20–60 keV band (4.3 ± 0.6 cps, or 29 mCrab, during MJD 52673.623–52673.641), we find that the source flux varies by a factor larger than 20.

4.2. Pulsations

During the *EPIC/PN* observation of 8 ks, the source count rate varied from 1 to 4 cps (Fig. 5). Furthermore, the variations occur periodically. By searching for modulations in the power spectrum and in the χ^2 distribution, we obtain a period of 912 ± 5 s at a χ^2 of ~ 600 for 30 bins per period (Fig. 7a). The pulse period is determined by the centre of a Gaussian fit to the χ^2 distribution, and the error is calculated using the procedure developed by Horne & Baliunas (1986) on Lomb-Scargle periodograms. The *EPIC/PN* pulse profile folded with a period of 912 s, illustrated in Fig. 7b, indicates a pulse fraction of $38 \pm 5\%$.

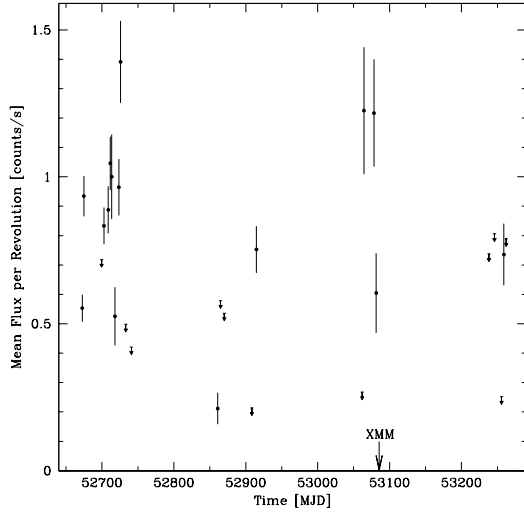


Fig. 4. *ISGRI* light curve (20–60 keV) of IGR J16393–4643 where each point represents the flux averaged over 1 spacecraft revolution. Upper limits (3σ) are provided when the source is not detected for an effective exposure time above 7 ks. The *XMM-Newton* observation (Fig. 5) occurred on MJD 53085.

For *ISGRI*, the pulse is best detected in the 100-s light curve of revolution 38 in the 15–40 keV band since this revolution has enough effective exposure time (50 ks) with low off-axis angles ($\sim 4^\circ$), and its light curve is free of gaps that hinder a periodicity search. Figure 6a presents the χ^2 distribution centered at 912 s, with 9 bins per period. The phase diagram is shown in Fig. 6b, and the pulse fraction is $57 \pm 24\%$. We merged the 100-s

Table 1. Source flux value (20–60 keV), significance, average off-axis angle, and exposure time when IGR J16393–4643 is detected at the 4σ level in the mosaic image of a spacecraft revolution. The median MJD of the visibility period is also given in reference to Fig. 4.

Visibility Period [Rev.]	Exp. [MJD]	Flux [ks]	Sig. [counts/s]	Angle [σ]	Angle [$^\circ$]
37	52672	204	0.55 ± 0.05	12.1	3.8
38	52675	92	0.93 ± 0.07	13.7	3.6
47	52703	153	0.83 ± 0.06	13.3	7.0
49	52709	85	0.89 ± 0.08	11.1	6.2
50	52712	104	1.05 ± 0.09	11.6	9.5
51	52714	76	1.00 ± 0.14	7.0	11.3
52	52718	93	0.53 ± 0.10	5.3	10.1
54	52724	100	0.96 ± 0.10	10.0	9.7
55	52726	96	1.39 ± 0.14	10.0	11.9
100	52861	205	0.21 ± 0.05	4.0	6.9
118	52915	146	0.75 ± 0.08	9.4	10.0
168	53064	28	1.22 ± 0.22	5.7	11.5
173	53078	27	1.22 ± 0.18	6.7	9.3
174	53081	53	0.60 ± 0.14	4.5	9.3
233	53259	72	0.74 ± 0.10	7.0	9.2

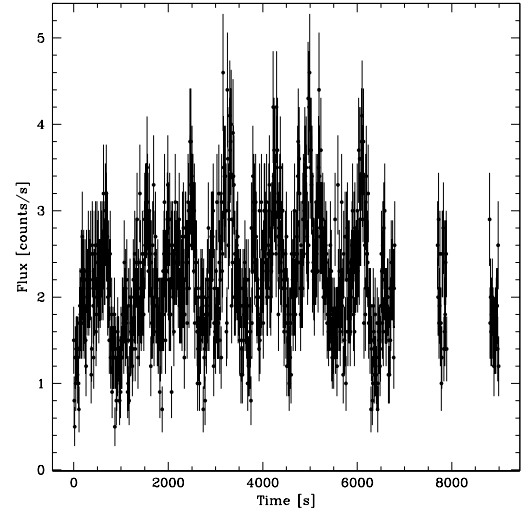


Fig. 5. *EPIC/PN* light curve for IGR J16393–4643 in the 2–10 keV energy range with a time resolution of 10 s. The observation starts at MJD 53085.37516.

light curves (15–30 keV) from revolutions 37–55, and derived a pulse period and error of 912.0 ± 0.1 s.

With respect to the pulse fractions, the amplitude does not change significantly as a function of energy. Both display a jagged rise to a peak flux followed by a drop. There appear to be primary and secondary peaks in the pulse profiles of both instruments at phases of ~ 0.7 and ~ 0.2 , respectively. Although the *ISGRI* and *EPIC* periods are derived from observations about 400 days apart, the period is not accurate enough to search for possible variations. In addition, the *ISGRI* light curves of revolutions that are nearly concurrent with the *EPIC* observation present low source significances which makes it difficult to search for a period.

There is an indication in the *EPIC* light curve (Fig. 5) that the source varies over timescales longer than the pulse period. At the beginning of the observation, the maximum of the pulse is about 3 cps. This maximum rises to 4 cps about 5 ks after the start time, and then decreases.

We did not detect an orbital period of the order of a few days in the combined *ISGRI* light curves (15–30 keV, 100-s resolution) of detected revolutions between 37 and 55.

5. Spectral Analysis

5.1. Average Spectrum

To extract an *ISGRI* spectrum, we created mosaics accumulating the data from revolutions 37–185 in the following energy bands; 22.09–25.92, 25.92–30.23, 30.23–40.28, 40.28–51.29, and 51.29–63.26 keV. These boundaries were chosen to conform with the current response matrices. The source is clearly detected up to 40 keV, so spectral bins at higher energies are ignored. A power law fit to the *ISGRI* spectrum returns a relatively steep photon index of 4.5 ± 0.4 ($\chi^2_\nu = 0.32$).

Spectral extraction for *EPIC/PN*, *EPIC/MOS1*, and *EPIC/MOS2* relied on single and double events within a cir-

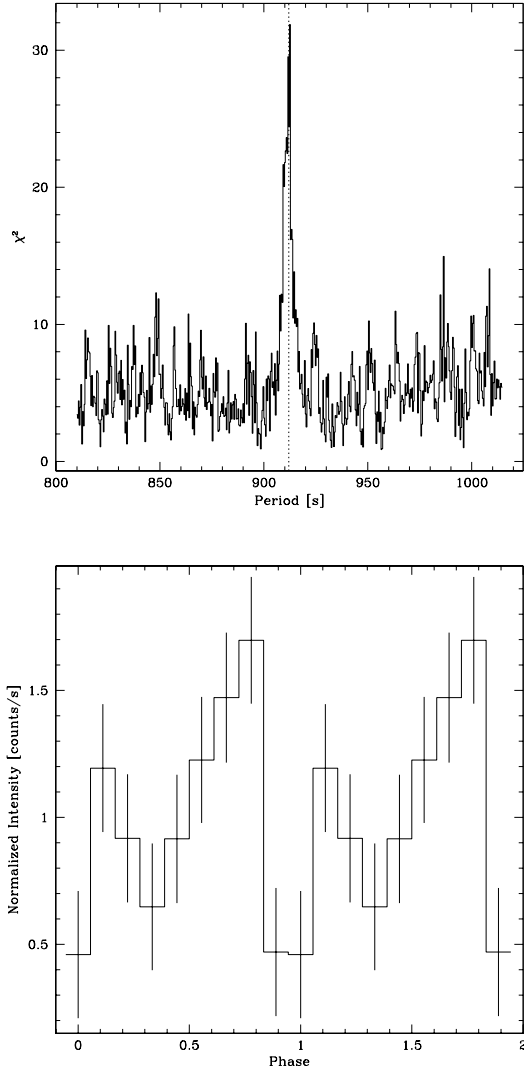


Fig. 6. *Top* (a): Period search (χ^2 distribution) on the *ISGRI* light curve (15–40 keV) of revolution 38, centred at 912 s (vertical line), with 9 bins per period, and a resolution of 0.4 s. *Bottom* (b): Pulse profile of the folded *ISGRI* light curve (15–40 keV) for a period of 912 s. The start time is MJD 52674.53833.

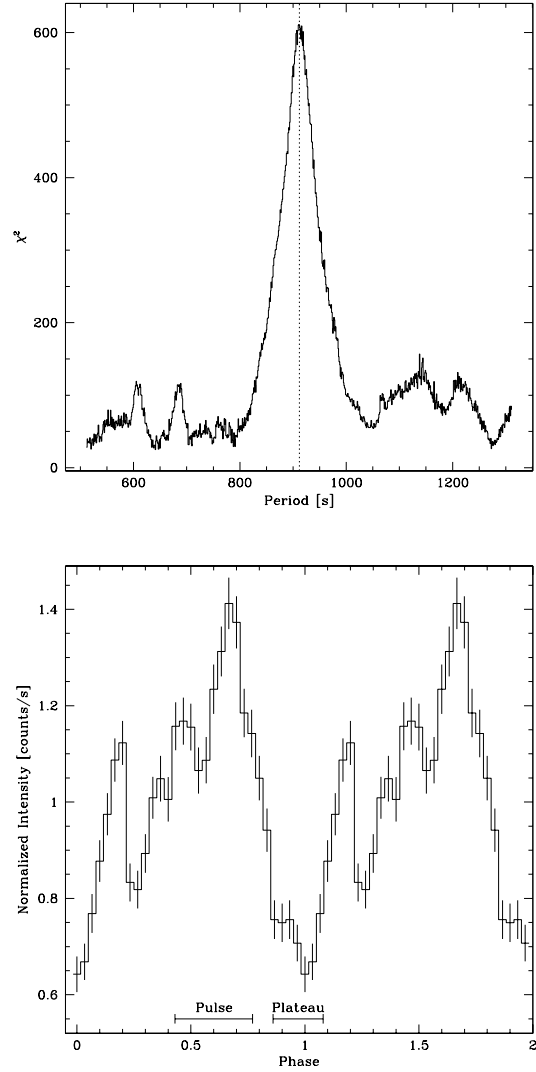


Fig. 7. *Top* (a): Distribution of χ^2 for the *EPIC/PN* 2–10 keV light curve with 30 bins per period, a resolution of 1 s, and centred at 912 s (vertical line). *Bottom* (b): Folded *EPIC/PN* light curve for a pulse period of 912 s beginning at MJD 53085.38738. The intervals indicate the pulse and plateau states of the phase-resolved spectrum.

cle of radius $25''$ centred on the source. To estimate the background, we made an event list from a circle of equal radius in the same detector and at an equivalent distance from the detector’s edge. Channels were configured to collect 30 counts per bin. An absorbed power law fit to the *EPIC* spectra has a photon index of 1.0 ± 0.1 with a column density of $3.1 \pm 0.1 \times 10^{23} \text{cm}^{-2}$ ($\chi^2_{\nu} = 1.15$).

The *EPIC* spectrum is heavily-absorbed below 4 keV. Iron emission lines appear at 6.4 keV (Fe K_{α}) and at 7.1 keV (Fe K_{β}). A discontinuity in the continuum above 7.1 keV suggests an iron absorption edge. There is an indication of an excess of soft emission between 0.5 and 2 keV. Including a soft blackbody component in an absorbed power law adjusted to the *EPIC* spectra decreases the χ^2 by 9 for 680 degrees of

freedom (dof), or a 0.5% probability that this feature is due to chance. Using a partial covering absorption instead of a blackbody raises the χ^2 by 60 for the same dof (679). A partially-ionised absorber is also insufficient to model the soft excess.

Simply fitting an absorbed power law to the spectra from *EPIC* and *ISGRI* yields $N_{\text{H}} \sim 4 \times 10^{23} \text{cm}^{-2}$ and $\Gamma \sim 2.3$, but the fit is poor ($\chi^2_{\nu} = 2.1$) with significant residuals in the hard X-rays. The *EPIC* photon index of 1.0 ± 0.1 is smaller than the one observed for *ISGRI* (4.5 ± 0.4) which indicates a spectral break. Such spectral shapes—a flat power law at low energies with a high-energy cutoff between 10–20 keV beyond which the slope steepens—are typical of X-ray pulsars (White et al. 1995).

We fit the combined *EPIC* and *ISGRI* spectra (Fig. 8) with a broken power law (BP), a power law with an exponential cutoff energy (CP), and a Compton emission (CE) model (`comptt` within *Xspec*). The models are modified by a galactic absorption in the direction of the source (fixed at $2.2 \times 10^{22} \text{cm}^{-2}$ (Dickey & Lockman 1990)), and an intrinsic photoelectric absorption with free iron abundances (Z_{Fe}). Soft excess emission is represented by a blackbody (with a fixed temperature of $kT_b = 0.06 \text{keV}$) that is affected by the galactic absorption only. Two narrow Gaussians (with widths fixed at 0) describe the iron lines. A constant (C_I) accounts for the asynchronous observations and for cross-calibration uncertainties.

The BP model ($\chi^2_{\nu}/\text{dof} = 0.95/675$) has photon indices of $\Gamma_1 = 0.9^{+0.1}_{-0.2}$ and $\Gamma_2 = 4.6^{+0.8}_{-0.3}$. However, the BP model does not constrain the break energy ($E_{\text{break}} > 17 \text{keV}$) nor C_I because it requires one more parameter than the other models. The CP model ($\chi^2_{\nu}/\text{dof} = 1.07/676$) gives $\Gamma = 0.8 \pm 0.2$, and a cutoff energy of $E_{\text{cut}} = 10 \pm 1 \text{keV}$, but residuals remain at high energy because of the low cutoff temperature. In Lutovinov et al. (2005a), an absorbed cutoff power law fit to the combined *ASCA* and *ISGRI* spectra had a comparable cutoff energy of $11 \pm 1 \text{keV}$, but the photon index was poorly constrained ($\Gamma = 1.3 \pm 1.0$).

Parameters from the CE model ($\chi^2_{\nu}/\text{dof} = 0.95/676$) are listed in Table 2. The column density (N_{H}) is $(25 \pm 2) \times 10^{22} \text{cm}^{-2}$. The comptonising medium has an electron temperature (kT_e) of $4.4 \pm 0.3 \text{keV}$ with an optical depth (τ) of 9 ± 1 . The Fe K_{α} line is at 6.41 ± 0.03 and has an equivalent width of $60 \pm 30 \text{eV}$ when measured with respect to the unabsorbed continuum, while the energy of the Fe K_{β} line is $7.1 \pm 0.1 \text{keV}$ with an equivalent width of $< 120 \text{eV}$. The detection of the K_{β} line is marginal given the uncertainties and its F-test probability of 3%. However, the ratio of iron intensities ($F_{K_{\beta}}/F_{K_{\alpha}}$) is consistent with the value expected from the photoionisation of iron (Kaastra & Mewe 1993). The absorbed, integrated fluxes (in units of $10^{-11} \text{ergs cm}^{-2} \text{s}^{-1}$) are 4.4 in the 2–10 keV band, and 5.1 in the 20–60 keV band. The observed soft excess flux between 0.5 and 2 keV is $7 \times 10^{-15} \text{ergs cm}^{-2} \text{s}^{-1}$. Since $C_I \sim 1$, the *EPIC* observation occurred during a period in which the source was in an average state.

5.2. Phase-resolved Spectrum

The *EPIC/PN* spectra were binned according to two states: a pulse state around the primary peak in the folded light curve (phase 0.43–0.77 in Fig. 7b), and a plateau state (phases 0.00–0.07 and 0.87–1.00). Average count rates for the pulse and plateau states are almost a factor of 2 apart at ~ 1.2 and ~ 0.7 , respectively. The CE model was applied to the phase-resolved *EPIC* spectra constrained with the *ISGRI* spectrum. Bins for the plateau gather 20 counts and bins for the pulse collect 40 counts per channel. The soft excess is not prominent in either spectrum so the blackbody component is omitted. This prevents an evaluation of the influence of the pulse on the soft excess. Table 2 reports parameters for the CE model fit to the phase-resolved spectra. The pulsation affects the normalisations but

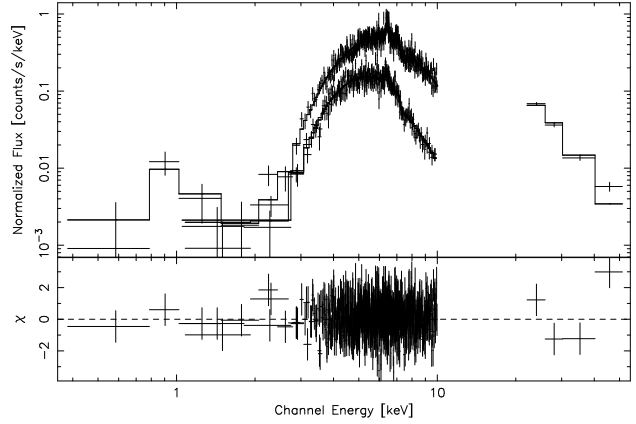


Fig. 8. Photon spectrum of IGR J16393–4643 from *EPIC/PN*, *EPIC/MOS1*, *EPIC/MOS2*, and *ISGRI*, fit with the comptonised continuum model (CE).

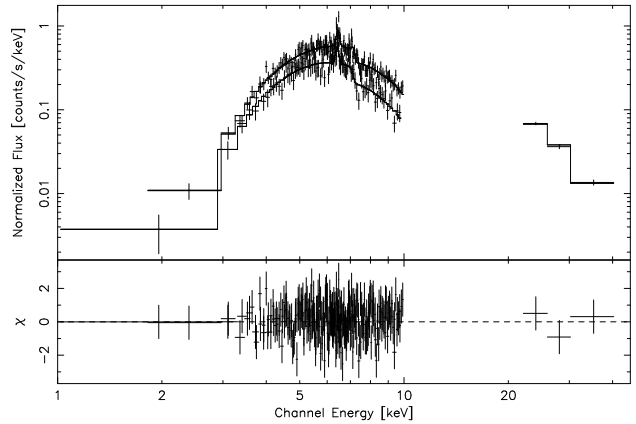


Fig. 9. Phase-resolved spectrum of IGR J16393–4643 from *EPIC/PN* during the pulse and plateau states. The *ISGRI* spectrum is included to constrain the CE model.

does not modify the shape of the spectra nor its parameters, specifically the N_{H} , in any appreciable way.

6. Discussion

Observations of IGR J16393–4643 by *INTEGRAL* and *XMM-Newton* present a source that is highly-obscured and persistent, with an intensity varying by a factor larger than 20. The source has a pulsation period of $912.0 \pm 0.1 \text{s}$. These attributes, along with its spectral shape, its neutral iron lines, and its lack of radio emission, suggest a HMXB system consisting of a magnetised neutron star orbiting inside the dense stellar wind of a supergiant companion. In the 2–10 keV energy band, the unabsorbed flux of IGR J16393–4643 is $9.2 \times 10^{-11} \text{ergs cm}^{-2} \text{s}^{-1}$. Assuming a luminosity of $1.2 \times 10^{36} \text{ergs s}^{-1}$, which is typical for accretion-driven X-ray pulsars (Bildsten et al. 1997), the source is located approximately 10 kpc away.

The absorbing column density is large whenever the source is detected, whether by *ASCA* ($N_{\text{H}} = 13^{+9}_{-7} \times 10^{22} \text{cm}^{-2}$), or now with *INTEGRAL* and *XMM-Newton* ($N_{\text{H}} = (25 \pm 2) \times 10^{22} \text{cm}^{-2}$). The strong absorption below 5 keV is intrinsic since it is an order of magnitude larger than the galactic absorption along the

Table 2. Parameters from the Compton emission (CE) model fit to the spectra of *EPIC* and *ISGRI* combined. Also listed are the values of the CE model (without a blackbody) fit to the pulse and plateau states of the phase-resolved *EPIC/PN* spectra constrained with the *ISGRI* spectrum. The integrated fluxes are listed as observed (F_{2-10}) or unabsorbed (F_{2-10}^{UA}). Errors denote 90% confidence.

Parameter	CE	Pulse	Plateau	Unit
C_I	0.8±0.2	0.6±0.2	1.3±0.7	
τ	9±1	12 ⁺⁶ ₋₂	8 ⁺⁴ ₋₂	
kT_e	4.4±0.3	4.4±0.3	4.4±0.4	keV
N_{H}	25±2	23 ⁺² ₋₆	24 ⁺³ ₋₇	10 ²² cm ⁻²
Z_{Fe}	1.0 ^{+0.4} _{-0.2}	0.9 ^{+0.6} _{-0.3}	1.2 ^{+0.8} _{-0.6}	Z_{\odot}
F_{2-10}	4.4	5.2	3.0	10 ⁻¹¹ ergs cm ⁻² s ⁻¹
F_{2-10}^{UA}	9.2	9.8	6.7	10 ⁻¹¹ ergs cm ⁻² s ⁻¹
$E_{K\alpha}$	6.41±0.03	6.44±0.03	6.41±0.04	keV
$F_{K\alpha}$	1.1±0.2	1.1±0.4	0.8±0.4	10 ⁻⁴ ph cm ⁻² s ⁻¹
$E_{K\beta}$	7.1±0.1	7.1±0.3	7.2±0.3	keV
$F_{K\beta}$	<0.62	<1.1	<1.3	10 ⁻⁴ ph cm ⁻² s ⁻¹
$\chi^2_{\nu}/\text{d.o.f.}$	0.95/676	0.92/140	0.92/94	

line of sight ($N_{\text{H}} = 2.2 \times 10^{22} \text{cm}^{-2}$). The absorption does not vary with the pulsation, which means that it is not related to the accretion column, but it may change with the orbital phase. This absorption indicates the presence of optically-thick material surrounding the compact object, which is consistent with the detection of iron lines.

Emission lines at 6.4 and 7.1 keV trace the quantity of matter in the shell that envelopes the neutron star. These lines are at the positions that would be expected from the fluorescence of cold neutral matter illuminated by continuum X-rays, and their equivalent widths are compatible with a spherical distribution of dense gas around the compact object (Matt 2002). A $K\alpha$ line at 6.41±0.03 keV ($\geq 1.925 \text{ \AA}$) corresponds to an ionisation of at most Fe XVIII (House 1969), which does not constrain the distance between the ionising source and the inner surface of the ionised shell. Given the errors on the line equivalent widths, we can not determine whether the fluxes of the iron lines are modified by the pulse.

There appears to be a soft excess flux of $7 \times 10^{-15} \text{ergs cm}^{-2} \text{s}^{-1}$ that is best represented by a blackbody rather than with a partial covering or partially-ionised absorber. The scattering of X-rays by the stellar wind is the most likely explanation for the soft excess emission (Haberl & White 1990). To what extent the pulse affects the soft excess emission is still unknown as the soft excess flux is not prominent in the phase-resolved spectrum.

The *ASCA* Faint Source Catalog (Sugizaki et al. 2001) listed IGR J16393–4643 among the brightest objects in its catalog, but the uncertainty of the position and the heavy absorption prevented Sugizaki et al. (2001) from associating this source with an optical counterpart. Malizia et al. (2004) noted the possible association between IGR J16393–4643 and the unidentified *EGRET* source 3EG J1639–4702 (Hartman et al. 1999). Non-thermal radio emission was recently detected within the *ASCA* error box (Combi et al. 2004) which suggests a dust-enshrouded microquasar and could help justify the *IBIS* and *EGRET* association. However, the *XMM-Newton*

position (R.A. (J2000)= 16^h39^m05.4^s, Dec.= -46°42′12″, 4″ uncertainty) is incompatible with the position of the radio source MOST J1639.0–4642, or any known radio source from the VizieR database. The pulsation and the lack of radio emission invalidate the microquasar interpretation for the HMXB. Also, the chance association of the *EGRET* source with IGR J16393–4643 is strong given the high density of sources in the region.

A single infrared candidate, 2MASS J16390535–4642137, lies within the *XMM-Newton* error circle of IGR J16393–4643. The high-energy spectral and timing characteristics of IGR J16393–4643 are reminiscent of other heavily-absorbed, wind-accreting X-ray pulsars with OB supergiant companions (Walter et al. 2004). A Be stellar companion is unlikely given that such systems are usually transient. Infrared observations should confirm the supergiant nature of the companion. If this is the case, it will constitute another argument rejecting the *EGRET* association (Orellana & Romero 2005).

Recently, combined *INTEGRAL* and *XMM-Newton* observations of the Norma Arm have revealed more pulsating X-ray binaries than were previously known. These objects have joined the ranks of what might be a new class of heavily-absorbed HMXBs that were previously undetected below 5 keV. The increasing sample size these objects represent should enable meaningful statistical studies to be performed. Understanding the nature of sources such as IGR J16393–4643 could shed light on the structure of stellar winds, provide constraints on the masses of neutron stars, and help elucidate the evolution of binaries.

Acknowledgements. The authors thank the anonymous referee for their prompt report which improved the paper. A. Bodaghee acknowledges J. Wendt, J. Rodriguez, A. Paizis, D. Willis, N. Produit and S. Paltani for their input and discussions. This research has made use of the SIMBAD database, operated at CDS, Strasbourg, France. This publication uses observations obtained with the ESA science missions *INTEGRAL* and *XMM-Newton*. The *INTEGRAL* and *XMM-Newton* instruments and data centres were directly funded by ESA member states and the USA (NASA).

References

- Bildsten, L., Chakrabarty, D., Chiu, J., et al. 1997, *ApJS*, 113, 367
- Bird, A. J., Barlow, E. J., Bassani, L., et al. 2004, *ApJ*, 607, L33
- Combi, J. A., Ribó, M., Mirabel, I. F., & Sugizaki, M. 2004, *A&A*, 422, 1031
- Courvoisier, T. J.-L., Walter, R., Beckmann, V., et al. 2003, *A&A*, 411, L53
- Cutri, R. M., Skrutskie, M. F., van Dyk, S., et al. 2003, *VizieR Online Data Catalog*, 2246, 0
- Dickey, J. M. & Lockman, F. J. 1990, *ARA&A*, 28, 215
- Ebisawa, K., Bourban, G., Bodaghee, A., Mowlavi, N., & Courvoisier, T. J.-L. 2003, *A&A*, 411, L59
- Haberl, F. & White, N. E. 1990, *ApJ*, 361, 225
- Hartman, R. C., Bertsch, D. L., Bloom, S. D., et al. 1999, *ApJS*, 123, 79
- Hill, A. B., Walter, R., Knigge, C., et al. 2005, *A&A*, 411, L53
- Horne, J. H. & Baliunas, S. L. 1986, *ApJ*, 302, 757
- House, L. L. 1969, *ApJS*, 18, 21
- Jansen, F., Lumb, D., Altieri, B., et al. 2001, *A&A*, 365, L1
- Kaastra, J. S. & Mewe, R. 1993, *A&AS*, 97, 443
- Lebrun, F., Leray, J. P., Lavocat, P., et al. 2003, *A&A*, 411, L141
- Liu, Q. Z., van Paradijs, J., & van den Heuvel, E. P. J. 2000, *A&AS*, 147, 25
- Lutovinov, A., Revnivtsev, M., Gilfanov, M., et al. 2005a, *A&A*, in press (astro-ph/0411550)
- Lutovinov, A., Rodriguez, J., Revnivtsev, M., & Shtykovskiy, P. 2005b, *A&A*, 433, L41
- Malizia, A., Bassani, L., di Cocco, G., et al. 2004, *The Astronomer's Telegram*, 227, 1
- Matt, G. 2002, *MNRAS*, 337, 147
- Monet, D. G., Levine, S. E., Canzian, B., et al. 2003, *AJ*, 125, 984
- Ochsenbein, F., Bauer, P., & Marcout, J. 2000, *A&AS*, 143, 23
- Orellana, M. & Romero, G. E. 2005, *Ap&SS*, 297, 167
- Rodriguez, J., Tomsick, J. A., Foschini, L., et al. 2003, *A&A*, 407, L41
- Strüder, L., Briel, U., Dennerl, K., et al. 2001, *A&A*, 365, L18
- Sugizaki, M., Mitsuda, K., Kaneda, H., et al. 2001, *ApJS*, 134, 77
- Turner, M. J. L., Abbey, A., Arnaud, M., et al. 2001, *A&A*, 365, L27
- Ubertini, P., Lebrun, F., Di Cocco, G., et al. 2003, *A&A*, 411, L131
- van Paradijs, J. 1983, in *Accretion-Driven Stellar X-ray Sources*, 189–260
- Voges, W., Aschenbach, B., Boller, T., et al. 1999, *A&A*, 349, 389
- Walter, R., Courvoisier, T. J.-L., Foschini, L., et al. 2004, in *The INTEGRAL Universe. Proceedings of the Fifth INTEGRAL Workshop. 16-20 February 2004, Munich, Germany*. Editor: B. Battrick, Scientific Editors: V. Schoenfelder, G. Lichti, & C. Winkler. ESA SP-552, Noordwijk: ESA Publication Division, ISBN 92-9092-863-8, 2004, p. 417-422., 417–422
- Walter, R., Rodriguez, J., Foschini, L., et al. 2003, *A&A*, 411, L427
- White, N. E., Nagase, F., & Parmar, A. N. 1995, *X-ray binaries (Cambridge Astrophysics Series, Cambridge, MA: Cambridge University Press, —c1995, edited by Lewin, Walter H.G.; Van Paradijs, Jan; Van den Heuvel, Edward P.J.)*, 1–57
- Winkler, C., Courvoisier, T. J.-L., Di Cocco, G., et al. 2003, *A&A*, 411, L1